HHS Public Access

Author manuscript

Magnetochemistry. Author manuscript; available in PMC 2021 June 03.

Published in final edited form as:

Magnetochemistry. 2020 December ; 6(4): . doi:10.3390/magnetochemistry6040058.

Ligand Control of ^{59}Co Nuclear Spin Relaxation Thermometry

Tyler M. Ozvat, **Spencer H. Johnson**, **Anthony K. Rappé**, **Joseph M. Zadrozny***

Department of Chemistry, Colorado State University, 1301 Center Ave., Fort Collins, CO 80523-1872, USA

Abstract

Studying the correlation between temperature-driven molecular structure and nuclear spin dynamics is essential to understanding fundamental design principles for thermometric nuclear magnetic resonance spin-based probes. Herein, we study the impact of progressively encapsulating ligands on temperature-dependent ^{59}Co T_1 (spin–lattice) and T_2 (spin–spin) relaxation times in a set of Co(III) complexes: $K_3[Co(CN)_6]$ (**1**); $[Co(NH_3)_6]Cl_3$ (**2**); $[Co(en)_3]Cl_3$ (**3**), en = ethylenediamine); $[Co(tn)_3]Cl_3$ (**4**), tn = trimethylenediamine); $[Co(tame)_2]Cl_3$ (**5**), tame = triaminomethylethane); and [Co(dinosar)]Cl_3 (**6**), dinosar = dinitrosarcophagine). Measurements indicate that ^{59}Co T_1 and T_2 increase with temperature for **1**–**6** between 10 and 60 °C, with the greatest $\Delta T_1/\Delta T$ and $\Delta T_2/\Delta T$ temperature sensitivities found for **4** and **3**, 5.3(3)% T_1/°C and 6(1)% T_2/°C, respectively. Temperature-dependent T_2* (dephasing time) analyses were also made, revealing the highest ΔT_2*/ΔT sensitivities in structures of greatest encapsulation, as high as 4.64% T_2*/°C for **6**. Calculations of the temperature-dependent quadrupolar coupling parameter, $\Delta e^2qQ/\Delta T$, enable insight into the origins of the relative $\Delta T_1/\Delta T$ values. These results suggest tunable quadrupolar coupling interactions as novel design principles for enhancing temperature sensitivity in nuclear spin-based probes.

Keywords

cobalt-59 NMR; magnetic relaxation; nuclear spins; quadrupolar interaction

* Correspondence: joe.zadrozny@colostate.edu.

Author Contributions: T.M.O., A.K.R., and J.M.Z. conceived of the experiments, T.M.O. and S.H.J. collected all reported experimental and computational data. All authors were involved in the composition of the manuscript. All authors have read and agreed to the published version of the manuscript.

Conflicts of Interest: There are no conflict of interest to report in this work.

Supplementary Materials: The following are available online at http://www.mdpi.com/2312-7481/6/4/58/s1, Figure S1: Variable-temperature inversion recovery fits of **1**, Figure S2: Variable-temperature inversion recovery fits of **2**, Figure S3: Variable-temperature inversion recovery fits of **3**, Figure S4: Variable-temperature inversion recovery fits of **4**, Figure S5: Variable-temperature inversion recovery fits of **5**, Figure S6: Variable-temperature inversion recovery fits of **6**, Figure S7: T_1 trend analysis ln(T_1) vs. T(°C) of **1**–**6**, Figure S8: Variable-temperature CPMG fits of **4** from 30–60 °C, Figure S9: Variable-temperature CPMG fits of **1** from 10–60 °C, Figure S10: Variable-temperature CPMG fits of **2** from 10–60 °C, Figure S11: Variable-temperature CPMG fits of **3** from 10–60 °C, Figure S12: Variable-temperature correlation times of **2**–**6**, Table S1: Variable-temperature ^{59}Co T_2* values and linewidth fit values, Table S2: Linear trend fit parameters for ln(T_1) vs $1/T$(10^3 K^{-1}) of **1**–**6**, Table S3: Calculated variable-temperature correlation times of **2**–**6**, Table S4: Computed structure of **3** at 13 °C, Table S5: Computed structure of **3** at 35 °C, Table S6: Computed structure of **3** at 57 °C, Table S7: Computed structure of **4** at 13 °C, Table S8: Computed structure of **4** at 35 °C, Table S9: Computed structure of **4** at 57 °C, Table S10: Computed structure of **5** at 13 °C, Table S11: Computed structure of **5** at 35 °C, Table S12: Computed structure of **5** at 57 °C, Table S13: Computed structure of **6** at 13 °C, Table S14: Computed structure of **6** at 35 °C, Table S15: Computed structure of **6** at 57 °C.

1. Introduction

The control of nuclear spin properties by molecular design is an important capability for many applications, spanning from diagnostic bioimaging [1–3] to encoding and processing quantum information [4–7]. A more focused application is designing temperature dependence into nuclear spin properties toward molecular-level thermometry, an essential technique for next-generation treatments of cancer [8–11]. Here, ^{59}Co nuclear spins are an extremely promising platform for detecting changes in temperature, owing to the extreme thermal sensitivity of the metal ion chemical shift [12]. We note that chemical shift is not the only temperature-dependent property of nuclear spins. Indeed, the influence of temperature on nuclear spin relaxation dynamics may provide a practical additional mechanism for thermometry. Importantly, the quadrupolar coupling of the ^{59}Co ($I = {}^{7}/_{2}$) nucleus is exquisitely sensitive to subtle changes in the structure of the coordination shell. Thus, slight temperature-dependent structural changes are expected to drive nuclear spin behaviors by manipulating the quadrupolar coupling interaction, inducing temperature dependence in the ^{59}Co spin–lattice and spin–spin relaxation times, T_1 and T_2, respectively. We note that other, more common nuclear spin-based probes, e.g., ^{1}H, ^{13}C, ^{19}F, and ^{31}P, are all $I = {}^{1}/_{2}$, are not quadrupolar nuclei, and thus do not sense changes in temperature in this manner [13–15].

Owing to the foregoing advantages, we target design strategies to control the temperature sensitivity of ^{59}Co nuclear spin dynamics in encapsulating ligands, which can prevent chemical decomposition in vivo, avoiding the release of toxic metal-ions [16–18]. Recent work by us demonstrated that the interconnected structures of encapsulating scaffolds amplify temperature sensitivity for contained ^{59}Co nuclei [19]. Importantly, these studies probed only temperature-driven changes in chemical shift. In contrast, it is unknown to what extent, if any, encapsulation affects the temperature dependence of ^{59}Co nuclear spin relaxation processes.

Herein, we provide the first test of the effect of encapsulation on the thermometric capabilities of the ^{59}Co nuclear spin dynamics in Co(III) complexes. To do so, we performed variable-temperature ^{59}Co NMR relaxation time experiments, specifically T_1, T_2, and linewidth analysis (T_2*) with a series of six octahedral and pseudo-octahedral cobalt(III) complexes: (Figure 1) $K_3[Co(CN)_6]$ (**1**); $[Co(NH_3)_6]Cl_3$ (**2**); $[Co(en)_3]Cl_3$ (**3**), en = ethylenediamine); $[Co(tn)_3]Cl_3$ (**4**), tn = trimethylenediamine); $[Co(tame)_2]Cl_3$ (**5**), tame = triaminomethylethane); and [Co(dinosar)]Cl_3 (**6**), dinosar = dinitrosarcophagine). This series enables comparison of the temperature-dependent relaxation dynamics of these complexes with (*i*) molecular symmetry (e.g., from the O_h complexes **1** and **2** to the nearly D_3 complexes **3–6**), and (*ii*) relative degree of encapsulation (from **2–6**). We further computed quadrupolar coupling parameters from computational structures to rationalize the relative temperature dependence of the relaxation dynamics. We find no precise correlation between relaxation and encapsulation. Instead, we propose that $\Delta T_1/\Delta T$ of the ^{59}Co nucleus is driven by changes in the quadrupolar coupling parameters, Δe^2qQ, from thermally driven structures. These evaluations highlight important structural conditions of chelation among the series, which are shown to yield various trends in temperature-dependent T_1, T_2, and T_2*.

2. Materials and Methods

2.1. General Considerations

Compounds utilized in this study were either purchased from commercial chemical vendors and used as received (**1** and **2**) or synthesized according previously reported literature preparations (**3**–**6**) [20–24].

2.2. Variable-Temperature ^{59}Co-NMR Spectroscopy

Samples of all measured compounds were made as 0.7 mL volumes of 30 mM concentrations in protiated distilled water. Spectroscopic measurements were made at 118 MHz (^{59}Co) using an Agilent Unity INOVA 500 MHz (^{1}H) spectrometer at a field strength of 11.74 T with a 5mm BB NMR probe. Before any data collection, standard shims, deuterium locking, and probe tuning were made on 1 M sample of $K_3[Co(CN)_6]$ in D_2O, the ^{59}Co-NMR reference standard. During ^{59}Co-NMR experiments, data were collected in the absence of shimming and locking due to field stability of the instrument. Each sample was measured across a temperature range of 10–60 °C in 10 °C intervals. For each regulated temperature interval, samples were allowed to thermally equilibrate for 15 min before the probe was tuned for each pulse experiment.

2.3. Variable-Temperature ^{59}Co Inversion Recovery and CPMG Experiments

Inversion recovery experiments were made on each sample across a temperature range of 10–60 °C in 10 °C intervals upon thermal equilibration. Inversion recovery data were acquired from 180°− τ − 90° pulse sequence experiments with 180° and 90° pulse lengths set at 22.4 and 11.2 μs, respectively. Pulse delay lengths τ were set by exponentially incremented time intervals relative to previously reported room temperature T_1 values of each compound [19]. Similarly, CPMG (Carr–Purcell–Meiboom–Gill) pulse sequence experiments were made on each sample across a temperature range of 10–60 °C in 10 °C increments [25,26]. CPMG data were acquired from 90° − $(\tau - 180° - \tau)_n$ spin echo pulse sequence experiments with 180° and 90° pulse lengths identical to the corresponding inversion recovery parameters.

2.4. Computation of ^{59}Co Quadrupolar Coupling Constants

Computational analyses were completed for the Co–N_6 encapsulation series (**2**–**6**) by structural optimizations over a range of temperatures. Temperature-specific optimizations were assisted by previous extended X-ray absorption fine-structure (EXAFS) characterization by fixing Co–N distances according to experimentally determined metal–ligand bond lengths to the three temperatures utilized in the EXAFS study, i.e., 13, 35, and 57 °C [27]. The remainder of the structure was allowed to optimize freely about the fixed Co–N_6 coordination sphere using the Gaussian 16 [28] electronic structure package. Electronic properties calculations were then performed using Orca 4.11 [29] to predict the quadrupolar coupling constant parameter (e^2qQ) of the temperature-specific optimized structures.

3. Results

The first temperature-dependent ^{59}Co nuclear spin property we investigated was the spin–lattice, or T_1, relaxation time. Variable-temperature inversion recovery experiments were performed for **1**–**6** over a 10–60 °C temperature range. At each temperature, an initially inverted ^{59}Co-NMR peak was observed and intensity was recovered as a function of increasing delay time following the inverting **π** pulse. Figure 2a shows the resulting recovery curves of **4** obtained from these pulsed experiments at different temperatures. Additional inversion recovery curves are available in the supplementary information (Figures S1–S6). The fitted inversion recovery data for **1**–**6** reveal lengthening of T_1 with increasing temperature. The observed ranges of T_1 span from 112.9(9) to 167(2) ms for **1**, 39.8(2) to 57(1) ms for **2**, 6.07(3) to 17.25(9) ms for **3**, 1.79(5) to 6.6(1) ms for **4**, 243(4) to 753(3) μs for **5**, and 264(7) to 682(2) μs for **6** (Figure 2c). The largest absolute change in T_1 over this temperature range is exhibited by **1** (ΔT_1 = 54(3) ms), while the smallest difference occurs for **6** (ΔT_1 = 408(9) μs). Between the minimum and maximum values of **1** and **6**, absolute changes in ΔT_1 for **2**–**5** are 17(1) ms, 11.2(1) ms, 4.8(2) ms, and 511(7) μs, respectively. The general magnitudes of these values are consistent with previous ^{59}Co relaxation data on structurally similar cobalt systems [30–33].

For the purpose of comparison, it is useful to define *relative* changes in T_1 for each complex since absolute differences ΔT_1, as above, heavily weight molecules with long T_1 times. As a result, the use of logarithmic scales of T_1 with temperature are necessary to show a clear comparison of ΔT_1 between **1**–**6** (Figure S7). In the following discussion, we express a comparative degree of change in T_1 between 10 to 60 °C as a percentage difference divided by the 50 °C window. For example, the ΔT_1 of **1** over 10 to 60 °C is approximately 54 ms. This value corresponds to a 48.2% increase in T_1 from 112.9 ms (10 °C) over the 50 °C window, thus quantitated by 0.96(6)% T_1/°C. Similarly, the other relative $\Delta T_1/\Delta T$ sensitivities are 0.86(6), 3.68(6), 5.3(3), 4.2(1), and 3.2(2)% T_1/°C for **2**–**6**, respectively. Figure 2b depicts the relative magnitudes of these values for all complexes over the 10–60 °C temperature window on a logarithmic scale. Owing to the potential utility of relaxation in modern biomedical imaging techniques, we highlight the aforementioned values of $\Delta T_1/\Delta T$ within the biologically relevant domain of 30–40 °C at 0.65(1), 0.70(1), 2.35(2), 2.98(9), 2.24(3), and 2.12(2)% T_1/°C for **1**–**6**, respectively (Figure 2c). These values follow the same general trend as with the 10–60 °C window, though the changes in magnitude differ slightly.

Notably, **4** shows the greatest change for both temperature windows, and **1** and **2** show the smallest relative increase in T_1. However, the relation between T_1 and T show varying degrees of temperature linearity across the series. T_1 is expected to show a linear temperature dependence if the quadrupolar mechanism is operative. A high degree of linearity is shown by the D_3-symmetric molecules of the series, **3**–**6**. For these complexes, quadrupolar relaxation is expected due to the interaction between the electric quadrupolar moment and the lower-symmetry electric field gradient at the ^{59}Co nucleus (relative to O_h **1** and **2**). However, the non-linear relaxation behaviors of **1** and **2** suggest different operative relaxation processes of the central ^{59}Co nucleus [30,34]. For these complexes, curvature in the plots of ln(T_1/s) vs. T (°C) (Figure 2b) show a gradual decline with increasing temperature, indicative of another contributing relaxation mechanism. The spin–rotation

relaxation mechanism is known to contribute to relaxation in similar O_h ^{59}Co complexes, [30,31] thus is the likely origin of the non-linear temperature dependence in **1** and **2**.

The second temperature-dependent nuclear spin property we investigated was T_2. Variable-temperature CPMG experiments were performed over a 10–60 °C temperature range for on **1**–**3**, and a 30–60 °C range for **4** to collect T_2 values. At each temperature measurement, a ^{59}Co NMR peak was observed with an intensity that decayed as a function of increasing number of π pulses. Figures S8–S11 show the resulting decay curves of the studied complexes and T_2 times were determined from exponential fits of the decay. Similar to the temperature-dependent T_1 behaviors, T_2 increases with increasing temperature for **1**–**4**. Figure 3a shows the relaxation trends for **1**–**4** over the 50 °C window. Unfortunately, due to instrumental limitations, we were not able to collect T_2 values for **4** at 10 and 20 °C, nor for **5** and **6** at any temperature between 10–60 °C. Pulse delay times for CPMG experiments on complexes with relatively low T_2 values approached the same timescales as the pulse durations (on the order of 10–20 μs). Thus, CPMG data could not be collected for **5** and **6**, which are likely to have even shorter T_2 times than **4** at 30 °C (the shortest experimentally determined T_2 value). For **1**–**4**, the observed range of T_2 times span from 102(3) to 132(3) ms for **1**, 9(1) to 32(6) ms for **2**, and 3.1(3) to 12.0(7) ms for **3** (Figure 3c). The largest absolute change in T_2 over a 10–60 °C temperature range is exhibited by **1** (ΔT_2 = 30(6) ms), followed by decreasing values of ΔT_2 at 23(7) ms for **2**, and 9(1) ms for **3**. Between 30–60 °C, T_2 for **4** was measured from 2.6(3) to 4.6(5) ms with an absolute ΔT_2 of 2.0(8) ms. The increases in T_2 over the studied range are expressed as $\Delta T_2/\Delta T$ by 0.6(1), 5(2), and 6(1)% T_2/°C over 10–60 °C for **1**–**3**, respectively, while an increase of 3(1)% T_2/°C is shown for **4** over 30–60 °C.

As an additional method of comparing the variation in ^{59}Co nuclear spin properties of **1**–**6**, we investigated the dephasing time, or T_2*, a relaxation time analogous to T_2 above. T_2* can be extracted from the temperature-dependent NMR linewidths through the relationship $T_2^* = 1/(2\pi\Delta\nu)$ where Δν (Hz) is the full width at half the maximum height (FWHM) of the ^{59}Co-NMR peak. This method enables a complete comparison of **1**–**6**, in contrast to the CPMG experiments. Figure 3b shows the temperature-dependent trends in T_2* for all complexes over the 10–60 °C range. Complexes **1**, **3**, and **4** all show increasing T_2* with increasing temperature up to a maximum, then begin to decrease with further increasing temperature. The maxima occur near 30, 20, and 40 °C for **1**, **3**, and **4**, respectively. In contrast, complex **2** shows a continual decline in T_2* over the studied temperature range, while **5** and **6** both exhibit linear increases in T_2*. The absolute changes in ΔT_2* over 10–60 °C are −2.27, −0.73, −1.06, 0.24, 0.39, and 0.40 ms for **1**–**6**, respectively (Table S1). This trend is reflected in the smaller, biologically relevant 30–40 °C window, where absolute ΔT_2* values are −2.99, −0.13, −0.46, 0.05, 0.08, and 0.08 ms. As with ΔT_1 and ΔT_2, the absolute difference in timescales heavily weights complexes with already long T_2* values. The relative changes according to $\Delta T_2^*/\Delta T$, which here describe essentially the temperature dependence of the spectral linewidth, are −0.76, −0.67, −0.72, 0.33, 3.21, and 4.64% T_2*/ 00B0C for **1**–**6**, respectively. The largest increase in T_2* is shown by **6**, with **5** showing the second largest increase. This trend is reflected in the narrowing linewidths observed in the ^{59}Co NMR spectra as a function of increasing temperature.

To assist in understanding the relaxation time data, we computed values of the quadrupolar coupling constant parameter (e^2qQ) for the Co–N_6 encapsulation series (**2**–**6**) at different temperatures within the 10–60 °C window. Predictions of e^2qQ were completed from partially optimized, variable-temperature structures following analyses from extended X-ray absorption fine-structure (EXAFS) spectroscopy [27]. Values of e^2qQ computed for these structures range from −1.861 to −1.910 MHz for **2**, 2.441 to 2.392 for **3**, 1.088 to 0.893 MHz for **4**, 8.165 to 8.156 MHz for **5**, and 6.879 to 6.834 MHz for **6** (Figure 4). The smallest values of e^2qQ are found for the smaller complexes (**2**–**4**) reflecting higher symmetries in molecular structure, relative to the larger, more encapsulating D_3 structures (**5** and **6**) showing the largest values of e^2qQ in the series.

The differences in e^2qQ by temperature-driven structure vary in scale, but all decrease with increasing temperature (Figure 4). Values of Δe^2qQ for **2**–**6** are found to be −0.049, −0.049, −0.195, −0.009, and −0.045 MHz, respectively. Of these predicted values, the greatest change is found for **4** followed by **2** and **3**, then **6** and **5**. Importantly, the largest Δe^2qQ is exhibited by **4** which also shows the largest $\Delta T_1/\Delta T$ value. Conversely, the encapsulated D_3 structures of **5** and **6** possess the highest magnitudes of e^2qQ between 8.156 to 8.165 MHz and 6.834 to 6.879 MHz, respectively, but show the least change by Δe^2qQ.

4. Discussion

Spin–lattice relaxation of the ^{59}Co nucleus is primarily attributed to the electric quadrupolar coupling interaction [30–32], which is dictated by the symmetry and structure of a given ligand shell. Evaluation of T_1 via Arrhenius analyses of **1**–**6** elucidate the extent to which this is true. In principle, a higher linearity of $\ln(T_1)$ vs. $1/T$ (10^3 K^{-1}) depicted in Figure 5 indicates the contribution of a single relaxation process in governing T_1. A slightly curved temperature dependence is observed for O_h **1** and **2**, as evidenced by the lower R^2 values (0.91) to linear regression. Conversely, highly linear trends are observed for the more D_3-symmetry **3**–**6**, with R^2 values of 0.99. For this latter series of four complexes, an activation energy, E_a, can be extracted from these linear fits to the Arrhenius equation, $1/T_1 = A \exp(-E_a/RT)$, where A is a preexponential factor, R is the ideal gas constant, and T is absolute temperature (Table S2). Here, E_a describes the activation energy to molecular tumbling, and a lower E_a suggests more facile motion in solution [30,35,36]. Activation energies for **3**–**6** are found to be 16.4(5), 20.6(3), 17.6(5), and 14.9(1) kJ/mol, respectively (1.37(4), 1.72(3), 1.47(4), and 1.24(1) × 10^3 cm^{-1}, respectively). Values of E_a increase from **6** < **3** < **5** < **4**, reflecting the same trend in $\Delta T_1/\Delta T$. Notably, the moderately encapsulated complex **4** shows the highest barrier to rotation and also the highest $\Delta T_1/\Delta T$. If the spin–lattice relaxation is expected to be driven by motional changes dependent on molecular mass, then the observed trend in $\Delta T_1/\Delta T$ cannot be strictly reasoned by changes in a temperature-dependent correlation time, τ_c (Figure S12 and Table S3). If the former were true, then the larger complexes **5** and **6** would be expected to have higher activation energies than that shown for **4**, an outcome that would be reflected by a longer τ_c in solution. In fact, they show shorter τ_c values, despite having larger ligand scaffolds. Thus, we conclude that the standard mechanisms for describing temperature-dependent relaxation, which principally stem from changes in correlation time, do not solely account for the observed changes here.

We instead propose that these changes in motion synergize with changes in the local symmetry of the ^{59}Co nucleus to produce the observed trends in $\Delta T_1/\Delta T$, especially in the series of D_3 structures. Previous studies of **3**–**6** revealed ~0.007 Å changes in Co–N bond distances per °C over the 50 °C temperature range of our investigations here [27]. These changes in bond distances were also accompanied by changes in symmetry of the coordination geometry through changes in N–Co–N angles. As a result of these changes in symmetry, we find in our calculations here that the quadrupolar coupling constants decrease with increasing temperature with a magnitude that trends as **4** > **3** > **6** > **5** (Figure 4). The trend in Δe^2qQ does not completely correlate to the trend in relaxation across the series, hence our suggestion that motion is also important. However, complex **4** shows *both* the greatest value of Δe^2qQ at −0.194 MHz, and the highest $\Delta T_1/\Delta T$ at 5.3(3)% $T_1/\Delta T$ over the 50 °C window.

The nearly equivalent values of T_1 and T_2 suggest that T_2 is limited by T_1, and, as such, T_2 is also expected to be impacted by the quadrupolar coupling. However, the temperature dependence of T_2 does not follow T_1. Owing to the large temperature dependence of the ^{59}Co chemical shift, we attribute this discrepancy to slight differences in resonance frequency by small temperature fluctuations which do not affect T_1 as strongly as T_2 [37]. We further highlight that the fast time scales of T_2 for **5** and **6** are beyond the limits of the instrumentation. Hence, it would be challenging to utilize T_2 as a thermometric parameter for these species. In that light, the temperature dependence of the ^{59}Co linewidth appears more favorable for thermometry in complexes of greater encapsulation (and thus most chemically stable) owing to the linearity of $\Delta T_2^*/\Delta T$ in the tridentate and encapsulated species **5** and **6**. Finally, we note that the values of T_2^* obtained here are likely lower bounds for this parameter, as temperature inhomogeneities in the instrument cavity (by even a fraction of 1 °C) will broaden the signal independent of T_2^*.

The above analyses suggest three important points for the development of ^{59}Co spin-based probes for quadrupolar-driven relaxation thermometry. Firstly, we note the importance of chelating or macrocyclic ligands, as **3**–**6** exhibited mostly quadrupolar relaxation, which is likely driven by the D_3-directing nature of these ligands. Secondly, we see that enabling a higher $\Delta T_1/\Delta T$ is largely dependent on whether the species possesses a strong temperature dependence of the quadrupolar coupling constant, not necessarily the magnitude of constant itself. Complex **4** exemplifies this point. Finally, third, the range of computed e^2qQ and Δe^2qQ imply a tunable quadrupolar coupling interaction through temperature-driven structures. It is worth noting that this is, to the best of our knowledge, the first argument for this effect in governing thermometry by relaxation. Moreover, in this context, the most-encapsulated structures, **5** and **6**, both show the lowest Δe^2qQ values, compared to the structures of **3** and **4** with lesser denticity. This effect may be rationalized by a hindered variation in the *symmetry* of the structure due to the relative interconnectivity of the individual N donor atoms. Indeed, EXAFS analyses suggest that **4** exhibits the greatest transition *towards* O_h symmetry with increasing temperature when **3**, **5**, and **6** all deviate toward D_3 symmetry [27]. This subtle difference in temperature-dependent structure is likely an important point toward designing future ^{59}Co NMR thermometers.

5. Conclusions

We report a collection of temperature-dependent relaxation dynamic studies on a series of progressively encapsulated cobalt(III) complexes. The foregoing temperature-dependent data underline the fact that structure plays a vital role in controlling relaxation thermometry for the ^{59}Co nucleus, but the coarse design principle of "encapsulation" does not solely govern the temperature dependence of T_1 nor T_2*. Relaxation times are found to be largely determined by the quadrupolar coupling interaction for the D_3 complexes and a combination of quadrupolar and spin–rotation mechanisms for the O_h species (**1** and **2**). The chelated complex **4** has the largest relative increase in T_1 as a function of its decrease in quadrupolar coupling, as mediated by a temperature-driven structure. We also found that encapsulated Co–N_6 species, demonstrated by **5** and **6**, are potentially promising thermometric structures by linear T_2* temperature dependencies. These factors thus provide a foundation for future studies of tuning temperature-dependent nuclear spin relaxation processes in Co(III) complexes.

Supplementary Material

Refer to Web version on PubMed Central for supplementary material.

Acknowledgments:

We acknowledge Z. Cleveland and C. Rithner for useful discussions and experimental assistance.

Funding: This research was performed with the support of Colorado State University (CSU) and the NIH (R21-EB027293). NMR experiments were performed on an instrument at the CSU Analytical Resources Core, which is supported by an NIH-SIG award (1S10OD021814–01) and the CSU-CORES Program. Computational resources are enabled by the Catalysis Collaboratory for Light-activated Earth Abundant Reagents (C-CLEAR), which is supported by the National Science Foundation (NSF) and the Environmental Protection Agency through the Networks for Sustainable Molecular Design and Synthesis (CHE-1339674) at Colorado State University, Fort Collins. S.H.J. acknowledges the Colorado Chapter of the ARCS Foundation for their continued support.

References

1. Sotoma S; Epperla CP; Chang H-C Diamond Nanothermometry. ChemNanoMat 2018, 4, 15–27.
2. Toyli DM; de las Casas CF; Christle DJ; Dobrovitski VV; Awschalom DD Fluorescence thermometry enhanced by the quantum coherence of single spins in diamond. Proc. Natl. Acad. Sci. USA 2013, 110, 8417–8421. [PubMed] [PubMed: 23650364]
3. Hui YY; Chen OY; Azuma T; Chang B-M; Hsieh F-J; Chang H-C All-Optical Thermometry with Nitrogen-Vacancy Centers in Nanodiamond-Embedded Polymer Films. J. Phys. Chem. C 2019, 123, 15366–15374.
4. Thiele S; Balestro F; Ballou R; Klyatskaya S; Ruben M; Wernsdorfer W Electrically driven nuclear spin resonance in single-molecule magnets. Science 2014, 344, 1135–1138. [PubMed: 24904159]
5. Gershenfeld NA; Chuang IL Bulk Spin-Resonance Quantum Computation. Science 1997, 275, 350–356. [PubMed: 8994025]
6. Havel TF; Cory DG; Lloyd S; Boulant N; Fortunato EM; Pravia MA; Teklemariam G; Weinstein YS; Bhattacharyya A; Hou J Quantum information processing by nuclear magnetic resonance spectroscopy. Am. J. Phys 2002, 70, 345–362.
7. Vandersypen LM; Steffen M; Breyta G; Yannoni CS; Sherwood MH; Chuang IL Experimental realization of Shor's quantum factoring algorithm using nuclear magnetic resonance. Nature 2001, 414, 883–887. [PubMed: 11780055]
8. Brace C Thermal Tumor Ablation in Clinical Use. IEEE Pulse 2011, 2, 28–38.

9. Tseng H; Lin S-E; Chang Y-L; Chen M-H; Hung S-H Determining the critical effective temperature and heat dispersal pattern in monopolar radiofrequency ablation using temperature-time integration. Exp. Ther. Med. 2016, 11, 763–768. [PubMed: 26997990]
10. Yuan J; Mei C-S; Panych LP; McDannold NJ; Madore B Towards fast and accurate temperature mapping with proton resonance frequency-based MR thermometry. Quant. Imaging Med. Surg. 2012, 2, 21–32. [PubMed: 22773966]
11. Van Rhoon GC; Wust P Introduction: Non-invasive thermometry for thermotherapy. Int. J. Hyperth. 2005, 21, 489–495.
12. Levy GC; Terry Bailey J; Wright DA A sensitive NMR thermometer for multinuclei FT NMR. J. Magn. Reson. 1980, 37, 353–356.
13. Bornais J; Brownstein S A low-temperature thermometer for ^{1}H, ^{19}F, and ^{13}C. J. Magn. Reson. 1978, 29, 207–211.
14. Quast H; Heubes M; Dunger A; Limbach H-H A high-precision carbon-13 shift thermometer for the temperature range 100–300 K. J. Magn. Reson. 1998, 134, 236–244. [PubMed] [PubMed: 9761699]
15. Zuo CS; Bowers JL; Metz KR; Nosaka T; Sherry AD; Clouse ME $TmDOTP^{5-}$: A substance for NMR temperature measurements in vivo. Magn. Reson. Med. 1996, 36, 955–959. [PubMed: 8946362]
16. Sargeson AM Developments in the synthesis and reactivity of encapsulated metal ions. Pure Appl. Chem. 1986, 58, 1511–1522.
17. Liu S; Li D; Huang C-W; Yap L-P; Park R; Shan H; Li Z; Conti PS The Efficient Synthesis and Biological Evaluation of Novel Bi-Functionalized Sarcophagine for ^{64}Cu Radiopharmaceuticals. Theranostics 2012, 2, 589–596. [PubMed: 22737194]
18. Liu S; Li Z; Conti PS Development of Multi-Functional Chelators Based on Sarcophagine Cages. Molecules 2014, 19, 4246–4255. [PubMed: 24705567]
19. Ozvat TM; Peña ME; Zadrozny JM Influence of ligand encapsulation on cobalt-59 chemical-shift thermometry. Chem. Sci. 2019, 10, 6727–6734. [PubMed: 31367328]
20. Krause R; Megargel E Student synthesis of tris(ethylenediamine)cobalt(III) chloride. J. Chem. Educ. 1976, 53, 667.
21. Bailar JC; Work JB Some Coördination Compounds of Cobalt Containing Trimethylenediamine and Neopentanediamine. J. Am. Chem. Soc. 1946, 68, 232–235.
22. Geue RJ; Snow MR Structure, conformational analysis and optical activity of a bis(tridentate)cobalt(III) complex. (+)589-ΔλλBis[1,1,1-tris(aminomethyl)ethane]cobalt(III) chloride (+)589-(R,R)-tartrate hydrate. Inorg. Chem. 1977, 16, 231–241.
23. Qin C-J; James L; Chartres JD; Alcock LJ; Davis KJ; Willis AC; Sargeson AM; Bernhardt PV; Ralph SF An Unusually Flexible Expanded Hexaamine Cage and Its CuII Complexes: Variable Coordination Modes and Incomplete Encapsulation. Inorg. Chem. 2011, 50, 9131–9140. [PubMed] [PubMed: 21806034]
24. Bottomley G; Clark I; Creaser I; Engelhardt L; Geue R; Hagen K; Harrowfield J; Lawrance G; Lay P; Sargeson A; et al. The Synthesis and Structure of Encapsulating Ligands: Properties of Bicyclic Hexamines. Aust. J. Chem. 1994, 47, 143–179.
25. Carr HY; Purcell EM Effects of Diffusion on Free Precession in Nuclear Magnetic Resonance Experiments. Phys. Rev. 1954, 94, 630–638.
26. Meiboom S; Gill D Modified Spin-Echo Method for Measuring Nuclear Relaxation Times. Rev. Sci. Instrum. 1958, 29, 688–691.
27. Ozvat TM; Sterbinsky GE; Campanella AJ; Rappé AK; Zadrozny JM EXAFS investigations of temperature-dependent structure in cobalt-59 molecular NMR thermometers. Dalton Trans. 2020.
28. Frisch MJ; Trucks GW; Schlegel HB; Scuseria GE; Robb MA; Cheeseman JR; Scalmani G; Barone V; Petersson GA; Nakatsuji H; et al. Gaussian 16 Rev. C.01; Gaussian, Inc.: Wallingford, CT, USA, 2016.
29. Neese F The ORCA program system. WIREs Comput. Mol. Sci. 2012, 2, 73–78.
30. Kirby CW; Puranda CM; Power WP Cobalt-59 nuclear magnetic relaxation studies of aqueous octahedral cobalt(III) complexes. J. Phys. Chem. 1996, 100, 14618–14624.

31. Ader R; Loewenstein A Nuclear magnetic relaxation studies in solutions of symmetric cobalt (III) complexes. J. Magn. Reson. 1969 1971, 5, 248–261.
32. Chacko VP; Bryant RG Electric field gradient modulation and nuclear magnetic relaxation in hexacyanocobaltate ion. J. Magn. Reson. 1984, 57, 79–84.
33. Doddrell DM; Bendall MR; Healy PC; Smith G; Kennard CHL; Raston CL; White AH ^{59}Co and ^{13}C Nuclear Spin Relaxation Studies in Solutions of Symmetric, Bidentate Cobalt(III) Complexes. On the Mechanism of ^{59}Co Spin Relaxation. Crystal Structure Determination of Tris(tropolonato)cobalt(III). Aust. J. Chem. 1979, 32, 1219–1230.
34. Boeré RT; Kidd RG Rotational Correlation Times in Nuclear Magnetic Relaxation. In Annual Reports on NMR Spectroscopy; Elsevier: Amsterdam, The Netherlands, 1983; Volume 13, pp. 319–385, ISBN 978–0-12–505313-6.
35. Foster RJ; Damion RA; Ries ME; Smye SW; McGonagle DG; Binks DA; Radjenovic A Imaging of nuclear magnetic resonance spin–lattice relaxation activation energy in cartilage. R. Soc. Open Sci. 2018, 5, 180221. [PubMed] [PubMed: 30109078]
36. Rieke V; Pauly KB MR Thermometry. J. Magn. Reson. Imaging 2008, 27, 376–390. [PubMed] [PubMed: 18219673]
37. Anet FAL; O'leary DJ The shielding tensor part II: Understanding its strange effects on relaxation. Concepts Magn. Reson. 1992, 4, 35–52.

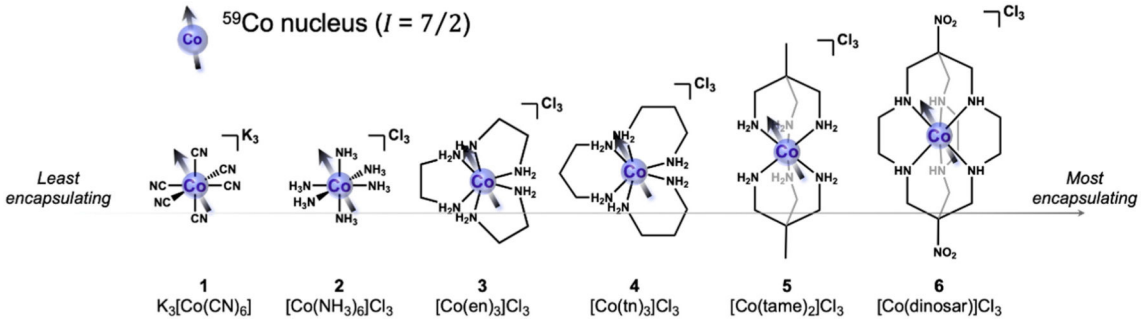

Figure 1.

Chemical structure series of low-spin octahedral cobalt(III) complexes. Complexes **2–6** make up the series of progressively encapsulated ^{59}Co nuclei by greater degrees of chelation in a common Co–N_6 coordination environment. Arrows represent the $I = {}^{7}/_{2}$ nuclear spin of the ^{59}Co nuclei in each complex. Hydrogens bound to carbons are omitted for clarity.

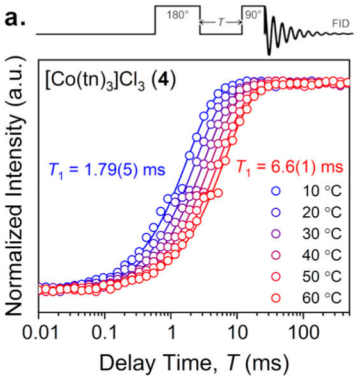

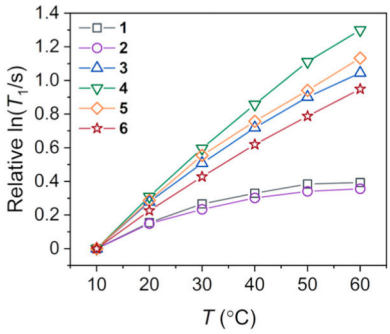

c.

	T_1 (ms)				T_1 (μs)	
T (°C)	1	2	3	4	5	6
10	112.9(9)	39.8(2)	6.07(3)	1.79(5)	243(4)	264(7)
20	131.8(9)	46.1(3)	8.02(3)	2.44(6)	323(3)	331(6)
30	147.3(9)	50.2(2)	10.09(5)	3.25(5)	423(4)	405(2)
40	156.9(9)	53.8(3)	12.46(6)	4.22(6)	517(2)	491(3)
50	166(1)	55.9(3)	15.0(1)	5.44(9)	622(3)	580(3)
60	167(2)	57(1)	17.25(9)	6.6(1)	753(3)	682(2)
ΔT_1	54(3)	17(2)	11.2(1)	4.8(2)	510(7)	408(9)

$\Delta T_1/\Delta T$ (%T_1/°C)						
T (°C)	1	2	3	4	5	6
10-60 °C	0.96(6)	0.86(6)	3.68(6)	5.3(3)	4.2(1)	3.2(2)
30-40 °C	0.65(1)	0.70(1)	2.35(2)	2.98(9)	2.24(3)	2.12(2)

Figure 2.

(**a**) Experimental variable-temperature (10–60 °C) inversion recovery measurements (circles) with exponential recovery fits (traces) for $[Co(tn)_3]Cl_3$ (**4**) on logarithmic scale. Temperature-specific T_1 values were extracted from exponential decay fits. The general pulse sequence for the inversion recovery experiment is depicted. (**b**) Variable-temperature T_1 plots of **1**–**6** on logarithmic scale showing relative changes. Error bars are within the width of the data points. Traces are guides for the eye. (**c**) Temperature-specific T_1 spin–lattice relaxation times with error for **1**–**6** from 10–60 °C with absolute values of ΔT_1 and relative values of $\Delta T_1/\Delta T$ temperature sensitivities.

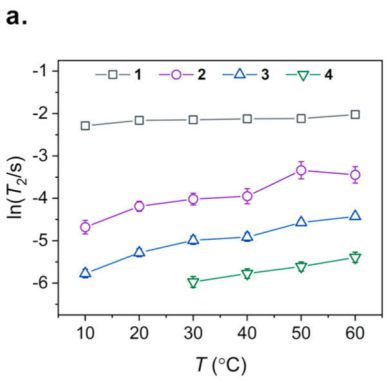

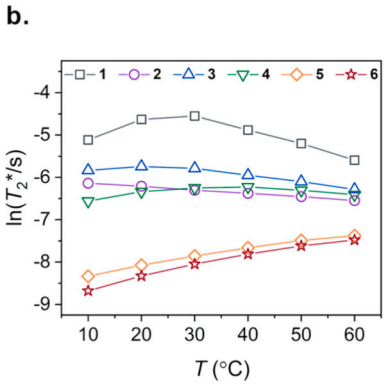

c.

T_2 (ms)				
T (°C)	1	2	3	4
10	102(3)	9(1)	3.1(3)	-
20	115(2)	15(2)	5.1(5)	-
30	117(4)	18(2)	6.8(7)	2.6(3)
40	120(3)	19(3)	7.4(7)	3.1(3)
50	120(3)	36(7)	10.4(7)	3.7(4)
60	132(3)	32(6)	12.0(7)	4.6(5)
ΔT_2	30(6)	23(7)	9(1)	2.0(8)

$\Delta T_2/\Delta T$ (%T_2/°C)				
T (°C)	1	2	3	4
10-60 °C	0.6(1)	5(2)	6(1)	-
30-60 °C	-	-	-	3(1)

Figure 3.

(**a**) Variable-temperature T_2 plots of **1**–**4** on logarithmic scale showing relative changes in T_2 spin–spin relaxation times. Error bars for $K_3[Co(CN)_6]$ (**1**) are within the width of the data points. Traces in both plots are mean to guide the eye. (**b**) Variable-temperature T_2* trends from linewidth analyses of **1**–**6** from 1D ^{59}Co NMR spectra. (**c**) Temperature-specific T_2 spin–spin relaxation times with error for **1**–**4** with absolute values of ΔT_2 and relative values of $\Delta T_2/\Delta T$ temperature sensitivities.

a.

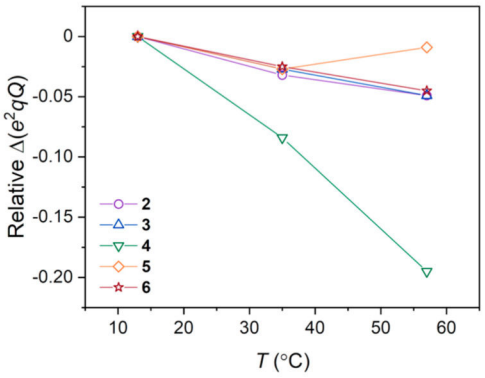

b.

Complex	e^2qQ (MHz) 13 °C	35 °C	57 °C	$\Delta(e^2qQ)$
2	-1.861	-1.893	-1.910	-0.049
3	2.441	2.414	2.392	-0.049
4	1.088	1.004	0.893	-0.195
5	8.165	8.138	8.156	-0.009
6	6.879	6.854	6.834	-0.045

Figure 4.

(**a**) Trends in predicted quadrupolar coupling parameters, e^2qQ, from variable-temperature predicted structures of **2**–**6**. (**b**) Temperature-specific quadrupolar coupling parameters at each temperature-specific structure and Δe^2qQ over the ~50 °C range.

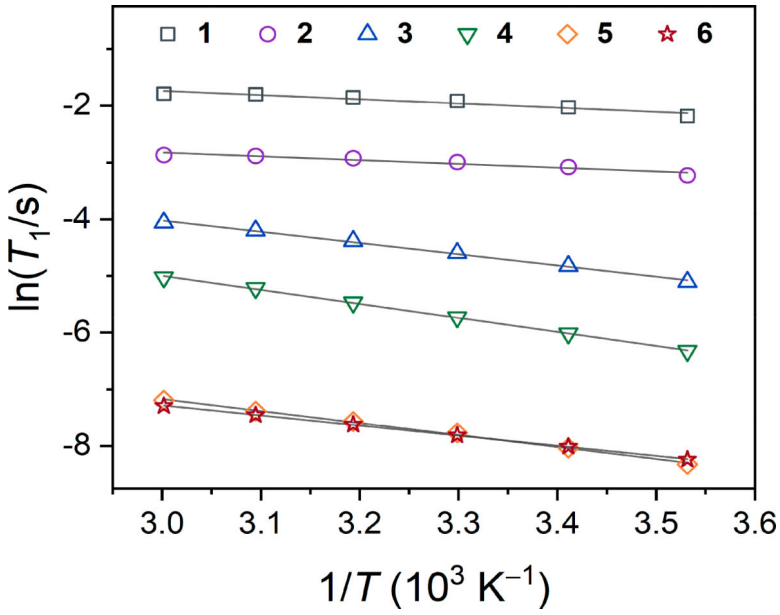

Figure 5.

Arrhenius plots of variable-temperature T_1 relaxation. Solid grey lines indicate linear regressions for **1–6**. Values of R^2 from each fit (Table S2) are used to determine temperature linearity for each complex.